

Coplanar cavity for strong coupling between photons and magnons in van der Waals antiferromagnet

Supriya Mandal,^{1,*} Lucky N. Kapoor,^{1,*} Sanat Ghosh,¹ John Jesudasan,¹ Soham Manni,^{1,2}
A. Thamizhavel,¹ Pratap Raychaudhuri,¹ Vibhor Singh,^{3,†} and Mandar M. Deshmukh^{1,‡}

¹*Department of Condensed Matter Physics and Materials Science,*

Tata Institute of Fundamental Research, Homi Bhabha Road, Mumbai 400005, India

²*Department of Physics, Indian Institute of Technology Palakkad, Palakkad 678557, India*

³*Department of Physics, Indian Institute of Science, Bangalore 560012, India*

We investigate the performance of niobium nitride superconducting coplanar waveguide resonators towards hybrid quantum devices with magnon-photon coupling. We find internal quality factors ~ 20000 at 20 mK base temperature, in zero magnetic field. We find that by reducing film thickness below 100 nm internal quality factor greater than 1000 can be maintained up to parallel magnetic field of ~ 1 T and perpendicular magnetic field of ~ 100 mT. We further demonstrate strong coupling of microwave photons in these resonators, with magnons in chromium trichloride, a van der Waals antiferromagnet, which shows that these cavities serve as a good platform for studying magnon-photon coupling in 2D magnonics based hybrid quantum systems. We demonstrate strong magnon-photon coupling for both optical and acoustic magnon modes of an antiferromagnet.

Superconducting coplanar waveguide (SCPW) resonators are of interest as elements of architecture for hybrid quantum systems and quantum computation related studies. The two dimensional (2D) structure, scalability and control over impedance across varying length scales for SCPW provide a natural way to couple them with various mesoscopic systems. They have been used for making kinetic inductance detectors, [1] parametric amplifiers, [2, 3] and have been coupled to superconducting qubits, [4] nano-mechanical resonators, [5, 6] spin ensembles, [7–11] and quantum dots. [12, 13] They have become an important component for realizing hybrid quantum devices.

For application of SCPW resonators in hybrid quantum devices involving electron spin resonance (ESR) systems, [9, 14–16] nitrogen vacancy (NV) centers, [7, 8] and different topological systems, [17–19] performance under magnetic field is additionally required. Furthermore, with the advent of 2D magnetic materials [20] and possibility to utilize their unique properties in hybrid quantum designing schemes ~ 100 mT magnetic fields in arbitrary directions is required. This additional requirement for the SCPW resonators necessitates use of type-II superconductors having high upper critical magnetic field (H_{C2}) like Mo-Re, TiN, Nb-Ti-N and NbN. [21–25] In the presence of magnetic field, flux vortices are generated in these materials which cause dissipative vortex motion in presence of high frequency oscillatory currents. Moreover, reduction in Cooper pairs due to formation of normal cores of the vortices causes increase in kinetic inductance which causes a decrease in resonance frequency. [26] Control over this kind of vortex induced dissipation can be achieved through introduction of pinning sites to trap the vortices which can either be done by utilizing intrinsic disorder [27] or by fabricating artificial pinning sites. [28–30]

Niobium nitride (NbN) is a disordered type-II supercon-

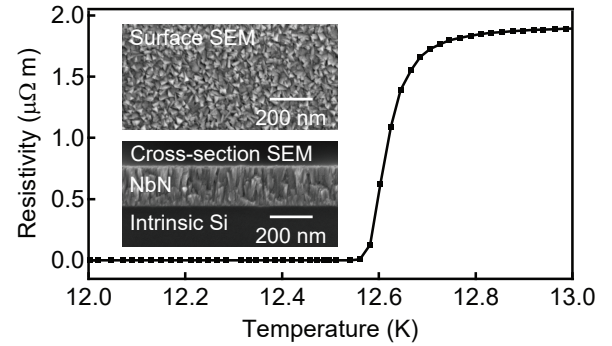


FIG. 1. Variation of resistivity of a 80 nm thick NbN film deposited by sputtering on intrinsic silicon with temperature [Inset: SEM images of top and cross sectional views of an NbN film].

ductor with a high transition temperature ($T_C \approx 16.8$ K), high upper critical magnetic field ($H_{C2} \approx 15$ T), small coherence length (≈ 5 nm) and large penetration depth (≈ 250 nm). [31–33] NbN thin films of varying thicknesses with moderately high T_C can be realized, which are also stable in ambient condition and robust with respect to thermal cycling from room temperature to cryogenic temperatures. Another interesting property of NbN is that its T_C depends mainly on the carrier density (and not disorder) for samples with $T_C > 10$ K. [31] This makes NbN a potential candidate for reducing dissipation due to vortices by utilizing inherent disorder.

In this work we fabricate and probe the properties of NbN SCPW resonators. Traditionally, SCPW resonators are fabricated by careful substrate surface preparation followed by the deposition of superconducting film. Subsequently, etching processes are used to pattern the resonator. Here we intentionally use a simple lift-off based fabrication process. The motivation behind this approach is two-fold: (a) it helps to establish baseline properties and (b) it opens up the possibility to integrate exfoliable materials into microwave circuitry. For these resonators we observe internal Q , Q_i of $\sim 2 \times 10^4$ at 20 mK temperature and zero magnetic field. We study the

* these authors contributed equally

† Corresponding author; v.singh@iisc.ac.in

‡ Corresponding author; deshmkh@tifr.res.in

magnetic field dependence of quality factor and resonance frequency dispersion of these resonators, primarily for two different thicknesses (t) of the NbN thin film. We find that Q_i is higher than 1000 for in-plane fields of ~ 1 T and perpendicular fields of ~ 100 mT. Few 100 mT is often the magnetic field range around which many materials show ferromagnetic, antiferromagnetic and electron spin resonances. [34–36] For example, using average g -factor of 2.2 for chromium trihalides [37] we find that approximately 160 mT magnetic field is required for resonant coupling of the magnons in these materials with microwave photons in a resonator with resonance frequency around 5 GHz. This makes NbN SCPW resonators an optimal platform for studying collective spin oscillations in different materials. Here we demonstrate coupling between a cavity mode in an NbN SCPW resonator and antiferromagnetic resonance (AFMR) modes in a chromium trichloride (CrCl_3) crystal – a van der Waals antiferromagnet. [34, 36]

We use intrinsic silicon as substrate for fabrication of the SCPW resonators (we also fabricated resonators on sapphire substrate and the corresponding characterization data is included in the supplementary material). First, the wafers are spin-coated with a bilayer resist consisting of EL9 and PMMA 950 A2. Subsequently, resonator pattern is made by electron beam lithography and developing in a solution of MIBK and IPA in 1:3 volume ratio. NbN is then deposited by reactive DC sputtering with a niobium (Nb) target at a sputtering power of 230 W in presence of continuous flow of 11 sccm of nitrogen and 70 sccm of argon at a sputtering pressure of 6.5×10^{-3} mbar and temperature 120 °C. [31] After sputtering, lift-off is done in acetone to remove the remaining resist along with excess NbN film on top of them. On an NbN film of thickness 80 nm, transport measurements give a $T_C \approx 12.5$ K, $H_C > 14$ T, RRR ≈ 0.9 and room temperature resistivity $\approx 1.95 \mu\Omega$ m. Variation of resistivity with temperature for the NbN film on intrinsic silicon substrate is shown in Fig. 1. Fig. 1 inset shows SEM image of an NbN film where disorder is clearly visible.

The SCPW resonators are designed in half-wave single port configuration. Fig. 2 (a) shows SEM image of the device. The resonator has a trace width of 28 μm and has been designed from a section of coplanar waveguide with characteristic impedance of 46 Ω on intrinsic silicon, neglecting the surface impedance of the superconducting film. A coupling capacitor is made between input port and the resonator for coupling microwave power in-and-out of the resonator. The measurements are done in a dilution fridge and sufficient number of attenuators are kept at different plates of the fridge in the input line to ensure proper thermalization of microwave photons reaching the sample (more details in the supplementary material).

Ratio of reflected to input signal for a one-port capacitively coupled resonator in reflection geometry, as seen in Fig. 2 (a), is described by the reflection coefficient S_{11} . Within the linear response of the resonator, S_{11} as a function of frequency, f ($= \frac{\omega}{2\pi}$), for a half-wave single port resonator can be modeled

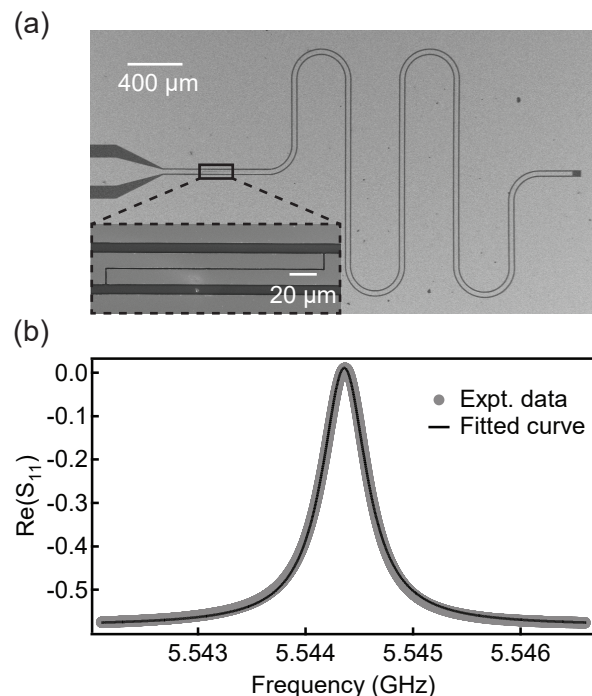


FIG. 2. (a) SEM image of an NbN SCPW resonator [Inset: Zoomed in image of coupling capacitor]. (b) Real part of S_{11} measured at 20 mK temperature along with fitting function.

by

$$S_{11}(\omega) = 1 - \frac{Q_i}{\frac{1}{2}(Q_i + Q_e) + iQ_iQ_e \frac{\omega - \omega_0}{\omega_0}} \quad (1)$$

where Q_i is the internal quality factor, Q_e is the external quality factor and f_0 ($= \frac{\omega_0}{2\pi}$) is the resonance frequency. [6] Fig. 2 (b) shows a representative measurement of the real part of S_{11} taken at 20 mK and zero magnetic field, along with the fitted curve using Eq. S1. This allows us to extract the Q_i for various studies done in this work. We find maximum $Q_i \approx 22000$ at 20 mK temperature and zero magnetic field. We note that Q_e determines the coupling of the resonator to the external measurement circuitry. We have studied resonators which are designed to be overcoupled ($Q_i > Q_e$) and undercoupled ($Q_i < Q_e$) at base temperature and zero magnetic field, to capture variation of Q_i in regimes with different internal loss rates. We have used the in-phase response (real part of S_{11}) to extract out the resonator parameters (details in the supplementary material).

As our primary motive is to develop these resonators for magnon coupling experiments, [35, 38, 39] it is imperative to characterize their response in magnetic field. Although the resonance frequency of a magnon mode depends on the geometry and the material properties, usually a magnetic field of ~ 100 mT could be sufficient to obtain magnon modes near 5 GHz. [34–36] Magnetic field dependence of the resonators in orientations parallel (B_{para}) and perpendicular (B_{perp}) to the SCPW plane has been shown in Fig. 3. Fig. 3 (a) and (b) show the color-scale plots of $|S_{11}|^2$ as a function of frequency and magnetic field for an NbN SCPW resonator, with film

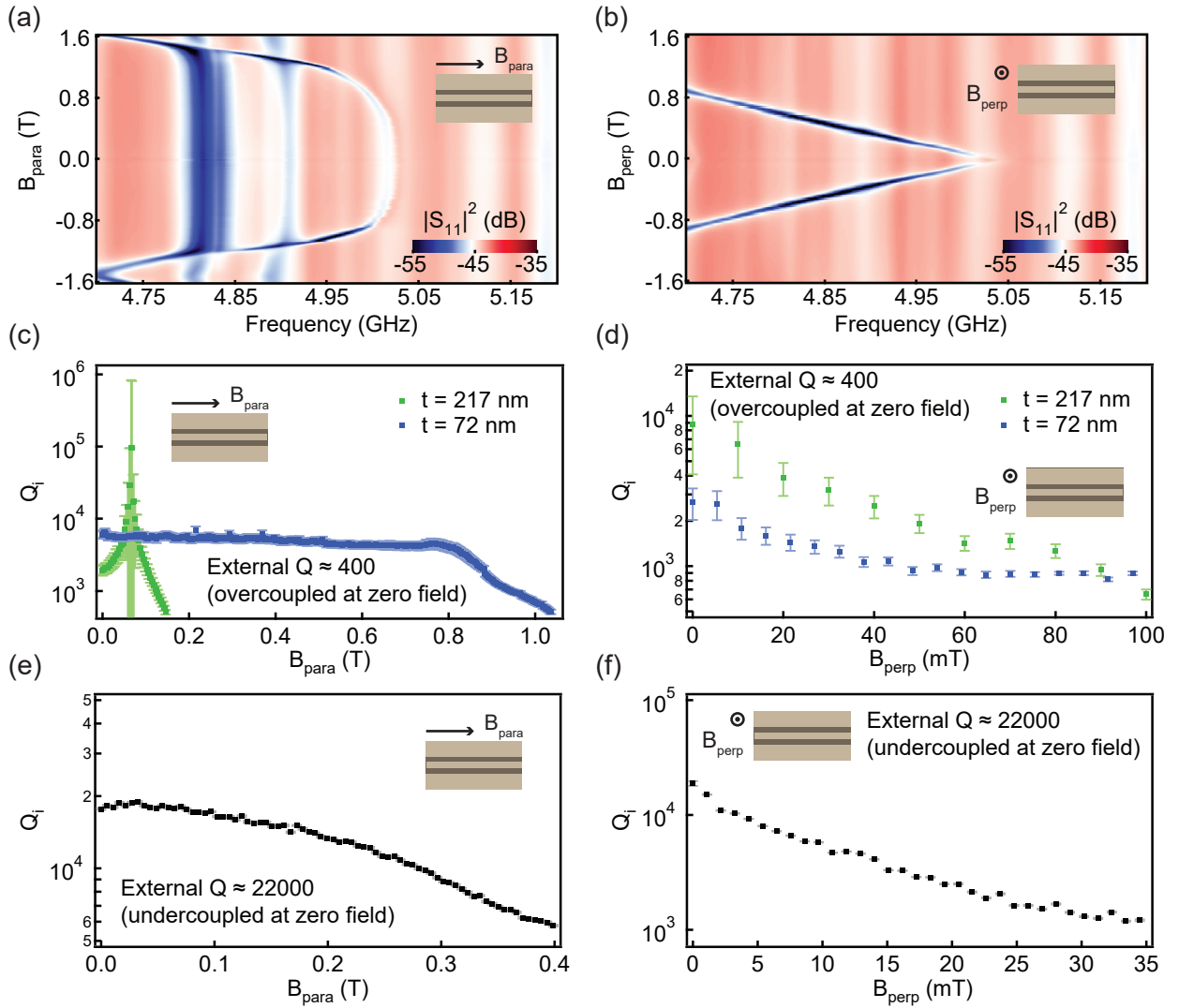


FIG. 3. Characterization of NbN resonators as a function of magnetic field. (a) and (b) Color-scale plots showing variation in $|S_{11}|^2$ for an NbN SCPW resonator with NbN film thickness 72 nm, with frequency and magnetic field for field orientations parallel and perpendicular to the SCPW plane respectively. (c) and (d) Variation of Q_i with magnetic field for film thicknesses 217 nm and 72 nm on intrinsic silicon substrate, for parallel and perpendicular field orientations respectively. These resonators are overcoupled, $Q_i \gg Q_e$, at zero magnetic field; Q_i reduces with increasing magnetic field due to vortex induced losses and eventually goes to undercoupled regime, $Q_i < Q_e$; in undercoupled regime $|S_{11}|^2$ shows a dip at resonance frequency, while for $Q_i \gg Q_e$, change in $|S_{11}|^2$ is minimal. Although Q_i can be tracked up to large magnetic field range using this choice of Q_e , it gives rise to high error-bars in fits for Q_i when $Q_i \gg Q_e$ (near zero field). Another set of resonators with $Q_i \lesssim Q_e$ are studied to accurately determine Q_i near zero field. Dependencies at lower fields are more accurately calculated using these undercoupled resonators having film thickness 80 nm and are shown in (e) and (f) for parallel and perpendicular magnetic fields respectively; here the error-bars have reduced to size comparable to the markers. Measurements were performed at 20 mK temperature.

thickness 72 nm, on intrinsic silicon substrate, for field orientations parallel and perpendicular to the SCPW plane. These measurements have been done in zero-field-cooled condition to address magnetic field induced losses while continuously varying magnetic field, as is required in many applications. Note that here the cavity is designed to be overcoupled at zero magnetic field. In overcoupled regime, $|S_{11}|^2$ shows small variations (however the resonance feature can be clearly seen in the phase response) and hence resonance dip is not visible at zero magnetic field. The dip starts appearing as vortex induced losses show up at higher fields.

Fig. 3 (c) and (d) show the Q_i values extracted from fit using Eq. S1 for resonators in magnetic field orientation parallel and perpendicular to the SCPW plane respectively. Resonators in parallel field show slower decrease in Q_i . This agrees with the fact that all the films have thicknesses below penetration depth. Whereas, for perpendicular field the rate of degradation of Q_i is much faster due to the dominant role of vortex dynamics induced losses over quasiparticle losses. [40]

Comparing the data for variation with magnetic field parallel to the SCPW plane, shown in Fig. 3 (c) for 217 nm and 72 nm thick NbN films, we note that the degradation of Q_i is

slower for the thinner film as dissipation due to vortex dynamics plays a lesser role and only quasiparticle losses are important; while for the thicker film this is not the case and there is an early onset of vortex dynamics induced losses. NbN films with smaller thicknesses maintain higher Q_i ($> 10^3$) up to higher parallel magnetic field $B_{\text{para}} \approx 1$ T due to lower flux creep. For orientation of magnetic field perpendicular to the plane of the film, $Q_i > 10^3$ is observed up to $B_{\text{perp}} \approx 100$ mT field.

In Fig. 3 (c) and (d) the resonators are overcoupled ($Q_i \gg Q_e$) at zero field. The choice of Q_e for this is good for tracking Q_i up to larger field range, but leads to high error-bars in fits for Q_i in regime of low internal loss, which is realized near zero magnetic field. So, for determining Q_i more precisely in low magnetic field regime, we fabricated another set of resonators with lower coupling capacitor such that $Q_i \lesssim Q_e$ at zero field. Fig. 3 (e) and (f) show the result of analysis for Q_i with this Q_e and we notice that these results are consistent and have smaller fitting errors (additional details in the supplementary material).

The near quadratic and linear dispersion trends in Fig. 3 (a) and (b), in orientations parallel and perpendicular to the magnetic field respectively, is well described by Abrikosov-Gor'kov (AG) theory. [41] For SCPW resonators, resonance frequency of the fundamental mode can be written as $f_0 = \frac{\beta}{\sqrt{L_l}}$, where $\beta = \frac{1}{2l\sqrt{C_l}}$ with l , C_l and L_l being the length, capacitance per unit length and inductance per unit length of the resonator. The total inductance contains contribution from the geometric inductance (L_g , per unit length) and the kinetic inductance (L_k , per unit length). As the shift in resonance frequency comes from the kinetic inductance part, it is straight forward to obtain $\frac{\Delta L_k}{L_k} = -\frac{2\beta^2}{\beta^2 - f_0^2 L_g} \frac{\Delta f_0}{f_0}$ where Δ represents change in associated quantity from its $B = 0$ T value (here Δf_0 is shift in resonance frequency from its value at base temperature and zero magnetic field, $f_{0,0}$). Now we use the fact that for $T \ll T_C$, $L_k \propto \frac{1}{T_C}$ and $k_B \Delta T_C = -\frac{\pi\alpha}{4}$ where α is the half of depairing energy and for a thin film in perpendicular magnetic field case it can be written as $\alpha = DeB_{\text{perp}}$ where D is the electronic diffusion constant and e is magnitude of electron charge. [41, 42] Using this formalism we fit a straight line $\frac{\Delta f_0}{f_0} = -kB_{\text{perp}}$ to the dispersion (details in the supplementary material) and find D from the relation $D = \frac{8k}{\pi e} \frac{\beta^2 k_B T_C}{\beta^2 - f_0^2 L_g}$. We find $D \approx 5 \times 10^{-4} \text{ m}^2\text{s}^{-1}$ which is close to values reported previously. [43]

We observe a weak hysteresis in the measurement depending on the sweep direction of the magnetic field (details in the supplementary material). All the measurements presented in Fig. 3 were recorded consistently with an upward sweep direction of the magnetic field. In parallel field orientation, a misalignment between the direction of the magnetic field and the plane of the superconducting film, can also cause losses due to a non-zero out of plane component of the magnetic field. In our experiment, we estimated this misalignment to be less than 1° , as the shift in resonant frequency remains flat for parallel magnetic field up to ≈ 0.8 T. We also characterized the resonators as a function of temperature and microwave power,

and the details are provided in the supplementary material.

For application of the NbN SCPW resonators towards cavity magnonics devices, we investigated their coupling with magnons in CrCl_3 crystal, a van der Waals antiferromagnet. First, the microwave absorption spectroscopy of CrCl_3 was performed using a 20-30 μm thick CrCl_3 crystal flake placed on a coplanar waveguide type transmission line made out of copper on a printed circuit board (PCB) (measurement setup shown in supplementary material). The crystal was transferred to the PCB inside a glove-box and covered with Apeizon N grease to protect against ambient. This measurement was done in a cryostat under continuous flow of helium vapor, at a temperature of 1.5 K. On applying a magnetic field oriented parallel to the plane of the PCB and perpendicular to the direction of RF current in the transmission line, we observe two symmetry protected antiferromagnetic resonance modes with presence of a mode-crossing in the transmission spectra as shown in Fig. 4(a). The linearly dispersing mode (f_1) has been identified as the acoustic mode and the downward-going mode (f_2) has been identified as the optical mode. The two modes get excited when certain symmetry rules are satisfied. These modes and the symmetry arguments have been studied in detail in ref [34] and [36]. In our experiments, the DC magnetic field is always applied in the plane of the sample and perpendicular to the direction of the RF current. [34, 36] Using the derivative divide method[44], the data in Fig. 4(a) has been analyzed and the linewidth of the acoustic and optical modes have been determined as $\frac{\gamma_1}{2\pi} \approx 0.33$ GHz and $\frac{\gamma_2}{2\pi} \approx 0.42$ GHz respectively. The variation in these linewidths with magnetic field are found to be small.[36] We note that the optical mode has a broader linewidth compared to the acoustic mode.

After this, we placed a similar crystal flake at the current antinode of the NbN resonator on intrinsic Si chip inside glove-box and similarly covered with Apeizon N grease. This measurement was done in the dilution fridge and the grease provided additional benefit of good thermal anchoring of crystal to the 20 mK plate temperature. On applying magnetic field parallel to SCPW plane and perpendicular to the RF current direction at the current antinode, we observe formation of avoided crossing between the cavity mode and each of the two AFMR modes in the measured $|S_{11}|^2$, as shown in Fig.4 (b). This is the signature of strong magnon-photon coupling between microwave photons in the NbN resonator and antiferromagnetic magnons in CrCl_3 . Fig. 4 (c) shows line-plots at different magnetic fields. Frequency dispersion of the modes in Fig. 4 (b) and broader linewidth of the hybrid mode associated with the optical AFMR mode in Fig. 4 (c) agree with the results from the transmission spectroscopy measurement using the copper transmission line.

We further generated a plot of $|S_{11}|^2$ from calculation based on input-output theory. [14, 45, 46] According to this theory, the reflection coefficient (S_{11}) for the system with two non-interacting magnon modes coupled with a cavity photon mode

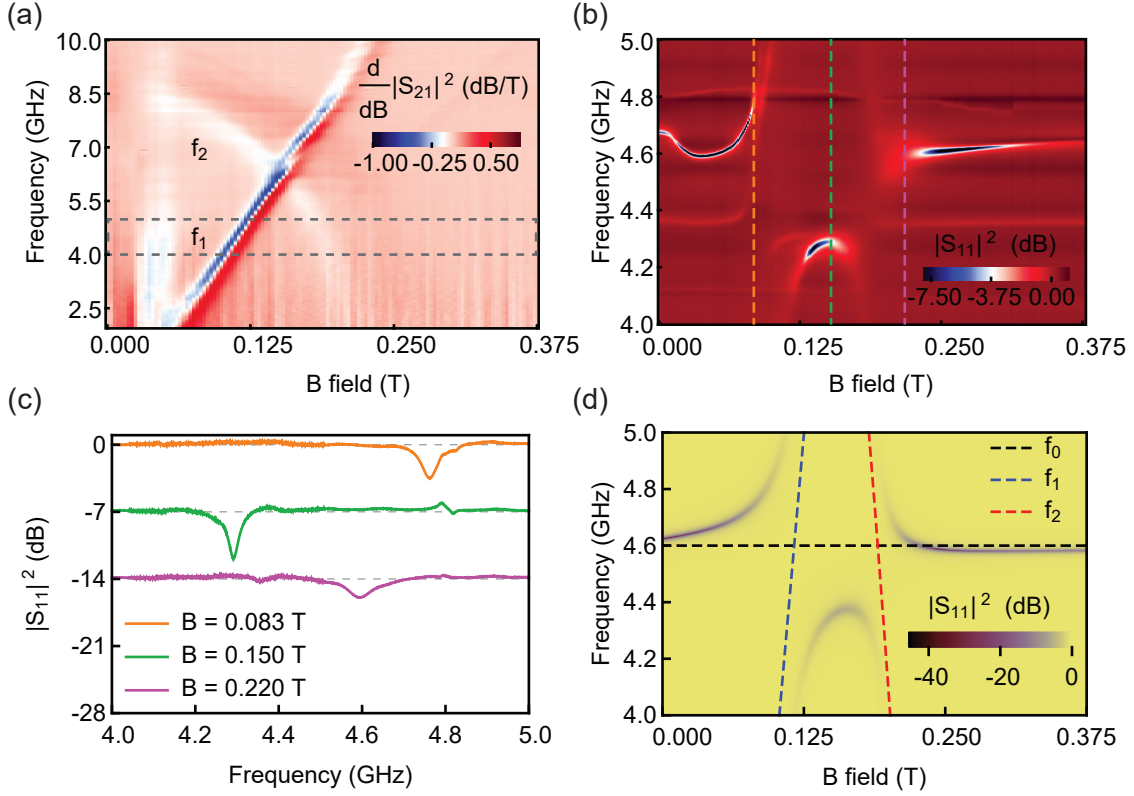


FIG. 4. Strong coupling between magnon modes in CrCl₃ and photon mode in NbN resonator. (a) Transmission spectra showing magnetic field dispersion of acoustic (f_1) and optical (f_2) AFMR modes in a CrCl₃ crystal flake placed on a copper coplanar waveguide transmission line. (b) Color-scale plot of the normalized $|S_{11}|^2$ with magnetic field and frequency for a CrCl₃ crystal flake placed at current antinode of an NbN SCPW resonator. The plot range is same as the gray dashed rectangle in (a) and shows the hybridization of the cavity mode with the acoustic and optical AFMR modes in CrCl₃ due to strong magnon-photon coupling. (c) Line-plots at three different fields (corresponding to dashed lines of same color in (b)). Offset of -7 dB has been added in consecutive plots for clarity. Line-shapes of upper hybrid modes, formed due to hybridization of cavity mode with acoustic and optical AFMR modes (orange and magenta, respectively), agree with the relatively broader line-width of optical mode compared to acoustic mode, as apparent from (a). (d) Plot of calculated $|S_{11}|^2$ using input-output theory with cavity mode of 0.57 GHz and 0.37 GHz respectively (dashed lines show the bare cavity (f_0), acoustic (f_1) and optical (f_2) AFMR modes).

can be written as

$$S_{11}(\omega) = 1 - \frac{\kappa_e}{i(\omega - \omega_0) + \frac{\kappa_i + \kappa_e}{2} + \frac{|g_1|^2}{i(\omega - \omega_1) + \frac{\gamma_1}{2}} + \frac{|g_2|^2}{i(\omega - \omega_2) + \frac{\gamma_2}{2}}} \quad (2)$$

where $\kappa_i = \frac{\omega_0}{Q_i}$ and $\kappa_e = \frac{\omega_0}{Q_e}$, $\frac{\omega_1}{2\pi} = f_1$ and $\frac{\omega_2}{2\pi} = f_2$ are the field dependent resonance frequencies of the acoustic and optical magnon modes respectively, $\frac{\gamma_1}{2\pi}$ and $\frac{\gamma_2}{2\pi}$ are their linewidths, and $\frac{g_1}{2\pi}$ and $\frac{g_2}{2\pi}$ are their coupling strength with the cavity mode respectively. For fitting the mode-coupling data shown in Fig. 4 (b), we defined a three mode coupling Hamiltonian matrix. The diagonal elements of this symmetric matrix comprises of the bare cavity mode, the bare acoustic magnon mode and the bare optical magnon mode. We keep the off-diagonal terms representing the coupling between cavity and acoustic mode, and between cavity and optical mode as fitting parameters, and take the cross coupling term between the two magnon modes to be zero. The field dependence of the acoustic and the optical modes were obtained from polynomial fits to the bare

magnon modes data shown in Fig. 4 (a), and the cavity mode was assumed to be constant in the field range considered. We use the field dependent functional forms of the eigenmodes of this matrix to perform a non-linear model fitting to the experimentally obtained mode-coupling data shown in Fig. 4 (d). This fitting gives $\frac{g_1}{2\pi} = 0.57$ GHz and $\frac{g_2}{2\pi} = 0.37$ GHz. Using these g values, we obtain the plot as shown in Fig. 4 (d) with the expression from input-output theory Eq. S2. The calculated cooperativity of coupling between acoustic magnon and photon, and between optical magnon and photon, using these values are $C_1 = \frac{g_1^2}{\kappa\gamma_1} = 47.10$ and $C_2 = \frac{g_2^2}{\kappa\gamma_2} = 15.59$ respectively, where $\kappa = \kappa_i + \kappa_e$. The cooperativities larger than the expected modes occupancy clearly suggest a quantum-coherent coupling between the photons and the magnons.

Since we use a CrCl₃ crystal covering almost the entire SCPW resonator, the effective volume for magnon-photon coupling is determined mainly by the magnetic mode volume of the resonator. From the lattice structure parameters of CrCl₃ and using the magnetic component of the vacuum

RF field of the resonator [38, 47], we calculate the coupling strength per spin to be $\frac{\hbar\omega}{2\pi} \approx 7.93$ Hz and a net coupling strength of ≈ 1.09 GHz for the estimated effective volume (more details regarding fitting and g value estimation is provided in the supplementary material). The deviation in the estimated and experimentally measured coupling rates could be attributed to reduction in the effective volume as predominantly the spins near the gap of resonator contribute to the measured signal. Also, coupling strength for the acoustic and the optical modes separately depend on both geometry and symmetry, as we observe them to be. A more accurate microscopic calculation and further experiments are needed to fully understand some aspects of the mode coupling data. This can be a focus of our future work. We also observe a faint dispersing mode below the main cavity mode in Fig. 4 (b) which also couples with the AFMR modes. This is possibly a parasitic mode of the resonator whose origin needs to be verified. Furthermore, a slight downward shift in cavity frequency with increasing magnetic field, seen between 10 mT and 30 mT, could possibly be attributed to the change in magnetic state of CrCl₃ as it undergoes spin-flop transition. [48–50] This measurement shows that our NbN resonators can be an ideal platform for studying collective spin oscillations and their coupling with electromagnetic modes of microwave frequencies in different systems.

In this work, we have fabricated NbN SCPW resonators using a simple fabrication process and probed their baseline properties. We see $Q_i > 10^3$ persisting up to perpendicular magnetic field of 100 mT which is two times higher than

the previously reported results. [30] Using substrate surface treatments and vortex trapping schemes Q_i of these resonators can be made even higher with better performance possibly up to even higher magnetic fields. Our fabrication protocols have the potential to incorporate exfoliable crystals in the microwave circuits. Furthermore, we have demonstrated the effectiveness of these resonators in coupling with spin ensembles by coupling them to magnons in a van der Waals anti-ferromagnetic system to study collective spin oscillations and making hybrid quantum devices.

See the supplementary material for details on measurement circuit, fitting procedure along with comparison between over-coupled and undercoupled resonators, characterization data for resonators on intrinsic silicon and sapphire substrate with temperature and microwave power, and details about magnon-photon coupling experiment.

We thank Rajamani Vijayaraghavan, Meghan Patankar, Ipsita Das, Sudhir Sahu, Suman Kundu, Sumeru Hazra, Ameya Riswadkar, Anirban Bhattacharjee and Srijita Das for helpful discussion and experimental assistance. We also thank Bhagyashree Chalke and Rudheer Bapat for doing SEM imaging. We acknowledge the Swarnajayanti Fellowship of the Department of Science and Technology (for M.M.D.), DST Nanomission grant SR/NM/NS-45/2016, SERB SUPRA SPR/2019/001247, ONRG grant N62909-18-1-2058, and the Department of Atomic Energy of the Government of India grant 12-R&D-TFR-5.10-0100 for support.

-
- [1] P. K. Day, H. G. LeDuc, B. A. Mazin, A. Vayonakis, and J. Zmuidzinas, *Nature* **425**, 817 (2003).
 - [2] E. A. Tholén, A. Ergül, E. M. Doherty, F. M. Weber, F. Grégis, and D. B. Haviland, *Applied Physics Letters* **90**, 253509 (2007).
 - [3] M. A. Castellanos-Beltran and K. W. Lehnert, *Applied Physics Letters* **91**, 083509 (2007).
 - [4] A. Wallraff, D. I. Schuster, A. Blais, L. Frunzio, R.-S. Huang, J. Majer, S. Kumar, S. M. Girvin, and R. J. Schoelkopf, *Nature* **431**, 162 (2004).
 - [5] C. A. Regal, J. D. Teufel, and K. W. Lehnert, *Nature Physics* **4**, 555 (2008).
 - [6] V. Singh, S. J. Bosman, B. H. Schneider, Y. M. Blanter, A. Castellanos-Gomez, and G. A. Steele, *Nature Nanotechnology* **9**, 820 (2014).
 - [7] Y. Kubo, F. R. Ong, P. Bertet, D. Vion, V. Jacques, D. Zheng, A. Dréau, J.-F. Roch, A. Auffeves, F. Jelezko, J. Wrachtrup, M. F. Barthe, P. Bergonzo, and D. Esteve, *Physical Review Letters* **105**, 140502 (2010).
 - [8] R. Amsüss, C. Koller, T. Nöbauer, S. Putz, S. Rotter, K. Sandner, S. Schneider, M. Schramböck, G. Steinhauser, H. Ritsch, J. Schmiedmayer, and J. Majer, *Physical Review Letters* **107**, 060502 (2011).
 - [9] V. Ranjan, G. de Lange, R. Schutjens, T. Debelhoir, J. P. Groen, D. Szombati, D. J. Thoen, T. M. Klapwijk, R. Hanson, and L. DiCarlo, *Physical Review Letters* **110**, 067004 (2013).
 - [10] A. Tkalčec, S. Probst, D. Rieger, H. Rotzinger, S. Wünsch, N. Kukharchyk, A. D. Wieck, M. Siegel, A. V. Ustinov, and P. Bushev, *Physical Review B* **90**, 075112 (2014).
 - [11] C. W. Zollitsch, K. Mueller, D. P. Franke, S. T. B. Goennenwein, M. S. Brandt, R. Gross, and H. Huebl, *Applied Physics Letters* **107**, 142105 (2015).
 - [12] J. R. Petta, A. C. Johnson, J. M. Taylor, E. A. Laird, A. Yacoby, M. D. Lukin, C. M. Marcus, M. P. Hanson, and A. C. Gossard, *Science* **309**, 2180 (2005).
 - [13] K. C. Nowack, F. H. L. Koppens, Y. V. Nazarov, and L. M. K. Vandersypen, *Science* **318**, 1430 (2007).
 - [14] D. I. Schuster, A. P. Sears, E. Ginossar, L. DiCarlo, L. Frunzio, J. J. L. Morton, H. Wu, G. A. D. Briggs, B. B. Buckley, D. D. Awschalom, and R. J. Schoelkopf, *Physical Review Letters* **105**, 140501 (2010).
 - [15] H. Malissa, D. I. Schuster, A. M. Tyryshkin, A. A. Houck, and S. A. Lyon, *Review of Scientific Instruments* **84**, 025116 (2013).
 - [16] O. W. B. Benningshof, H. R. Mohebbi, I. A. J. Taminiau, G. X. Miao, and D. G. Cory, *Journal of Magnetic Resonance* **230**, 84 (2013).
 - [17] F. E. Schmidt, M. D. Jenkins, K. Watanabe, T. Taniguchi, and G. A. Steele, *Nature Communications* **9**, 1 (2018).
 - [18] J. G. Kroll, W. Uilhoorn, K. L. v. d. Enden, D. d. Jong, K. Watanabe, T. Taniguchi, S. Goswami, M. C. Cassidy, and L. P. Kouwenhoven, *Nature Communications* **9**, 1 (2018).
 - [19] J. I.-J. Wang, D. Rodan-Legrain, L. Bretheau, D. L. Campbell, B. Kannan, D. Kim, M. Kjaergaard, P. Krantz, G. O. Samach, F. Yan, J. L. Yoder, K. Watanabe, T. Taniguchi, T. P. Orlando, S. Gustavsson, P. Jarillo-Herrero, and W. D. Oliver, *Nature Nanotechnology* **14**, 120 (2019).

- [20] C. Gong and X. Zhang, *Science* **363**, eaav4450 (2019).
- [21] V. Singh, B. H. Schneider, S. J. Bosman, E. P. J. Merkkx, and G. A. Steele, *Applied Physics Letters* **105**, 222601 (2014).
- [22] V. E. Calado, S. Goswami, G. Nanda, M. Diez, A. R. Akhmerov, K. Watanabe, T. Taniguchi, T. M. Klapwijk, and L. M. K. Vandersypen, *Nature Nanotechnology* **10**, 761 (2015).
- [23] D. J. van Woerkom, A. Geresdi, and L. P. Kouwenhoven, *Nature Physics* **11**, 547 (2015).
- [24] M. R. Vissers, J. Gao, D. S. Wisbey, D. A. Hite, C. C. Tsuei, A. D. Corcoles, M. Steffen, and D. P. Pappas, *Applied Physics Letters* **97**, 232509 (2010).
- [25] F. W. Carter, T. Khaire, C. Chang, and V. Novosad, *Applied Physics Letters* **115**, 092602 (2019).
- [26] C. Song, T. W. Heitmann, M. P. DeFeo, K. Yu, R. McDermott, M. Neeley, J. M. Martinis, and B. L. T. Plourde, *Physical Review B* **79**, 174512 (2009).
- [27] A. Ghirri, C. Bonizzoni, D. Gerace, S. Sanna, A. Cassinese, and M. Affronte, *Applied Physics Letters* **106**, 184101 (2015).
- [28] C. Song, M. P. DeFeo, K. Yu, and B. L. T. Plourde, *Applied Physics Letters* **95**, 232501 (2009).
- [29] D. Bothner, T. Gaber, M. Kemmler, D. Koelle, and R. Kleiner, *Applied Physics Letters* **98**, 102504 (2011).
- [30] J. Kroll, F. Borsoi, K. van der Enden, W. Uilhoorn, D. de Jong, M. Quintero-Pérez, D. van Woerkom, A. Bruno, S. Plissard, D. Car, E. Bakkers, M. Cassidy, and L. Kouwenhoven, *Physical Review Applied* **11**, 064053 (2019).
- [31] S. P. Chockalingam, M. Chand, J. Jesudasan, V. Tripathi, and P. Raychaudhuri, *Physical Review B* **77**, 214503 (2008).
- [32] M. Mondal, A. Kamlapure, M. Chand, G. Saraswat, S. Kumar, J. Jesudasan, L. Benfatto, V. Tripathi, and P. Raychaudhuri, *Physical Review Letters* **106**, 047001 (2011).
- [33] A. Kamlapure, M. Mondal, M. Chand, A. Mishra, J. Jesudasan, V. Bagwe, L. Benfatto, V. Tripathi, and P. Raychaudhuri, *Applied Physics Letters* **96**, 072509 (2010).
- [34] D. MacNeill, J. T. Hou, D. R. Klein, P. Zhang, P. Jarillo-Herrero, and L. Liu, *Physical Review Letters* **123**, 047204 (2019).
- [35] X. Zhang, C.-L. Zou, L. Jiang, and H. X. Tang, *Physical Review Letters* **113**, 156401 (2014).
- [36] L. N. Kapoor, S. Mandal, P. C. Adak, M. Patankar, S. Manni, A. Thamizhavel, and M. M. Deshmukh, *Advanced Materials* **33**, 2005105 (2021).
- [37] H. H. Kim, B. Yang, S. Li, S. Jiang, C. Jin, Z. Tao, G. Nichols, F. Sfigakis, S. Zhong, C. Li, S. Tian, D. G. Cory, G.-X. Miao, J. Shan, K. F. Mak, H. Lei, K. Sun, L. Zhao, and A. W. Tsen, *Proceedings of the National Academy of Sciences* **116**, 11131 (2019).
- [38] H. Huebl, C. W. Zollitsch, J. Lotze, F. Hocke, M. Greifenstein, A. Marx, R. Gross, and S. T. B. Goennenwein, *Physical Review Letters* **111**, 127003 (2013).
- [39] Y. Tabuchi, S. Ishino, T. Ishikawa, R. Yamazaki, K. Usami, and Y. Nakamura, *Physical Review Letters* **113**, 083603 (2014).
- [40] S. Kwon, A. Fadavi Roudsari, O. W. B. Benningshof, Y.-C. Tang, H. R. Mohebbi, I. A. J. Taminiiau, D. Langenberg, S. Lee, G. Nichols, D. G. Cory, and G.-X. Miao, *Journal of Applied Physics* **124**, 033903 (2018).
- [41] M. Tinkham, *Introduction to Superconductivity*, Dover Books on Physics Series (Dover Publications, 2004).
- [42] N. Samkharadze, A. Bruno, P. Scarlino, G. Zheng, D. P. DiVincenzo, L. DiCarlo, and L. M. K. Vandersypen, *Physical Review Applied* **5**, 044004 (2016).
- [43] M. Mondal, A. Kamlapure, S. C. Ganguli, J. Jesudasan, V. Bagwe, L. Benfatto, and P. Raychaudhuri, *Scientific Reports* **3**, 1357 (2013).
- [44] H. Maier-Flaig, S. T. B. Goennenwein, R. Ohshima, M. Shiraishi, R. Gross, H. Huebl, and M. Weiler, *Review of Scientific Instruments* **89**, 076101 (2018).
- [45] E. Abe, H. Wu, A. Ardavan, and J. J. L. Morton, *Applied Physics Letters* **98**, 251108 (2011), publisher: American Institute of Physics.
- [46] A. A. Clerk, M. H. Devoret, S. M. Girvin, F. Marquardt, and R. J. Schoelkopf, *Reviews of Modern Physics* **82**, 1155 (2010).
- [47] N. J. Lambert, J. A. Haigh, and A. J. Ferguson, *Journal of Applied Physics* **117**, 053910 (2015).
- [48] A. Narath and H. L. Davis, *Physical Review* **137**, A163 (1965).
- [49] M. A. McGuire, G. Clark, S. KC, W. M. Chance, G. E. Jellison, V. R. Cooper, X. Xu, and B. C. Sales, *Physical Review Materials* **1**, 014001 (2017).
- [50] B. Kuhlow, *physica status solidi (a)* **72**, 161 (1982).
- [51] J. Gao, M. Daal, A. Vayonakis, S. Kumar, J. Zmuidzinas, B. Sadoulet, B. A. Mazin, P. K. Day, and H. G. Leduc, *Applied Physics Letters* **92**, 152505 (2008).
- [52] D. Bothner, T. Gaber, M. Kemmler, D. Koelle, R. Kleiner, S. Wünsch, and M. Siegel, *Physical Review B* **86**, 014517 (2012).
- [53] L. Ji, M. S. Rzchowski, N. Anand, and M. Tinkham, *Physical Review B* **47**, 470 (1993).
- [54] P. Raychaudhuri, *Superconductor Science and Technology* **9**, 447 (1996).

SUPPLEMENTARY MATERIAL

SI. SCHEMATIC FOR MEASUREMENT CIRCUIT

Fig. S1 (a) shows schematic of the circuit for reflection measurement of the NbN SCPW resonators. Measurements are done in an Oxford Triton dilution fridge containing a superconducting magnet. Input line of the RF signal includes several attenuators at different stages of the fridge as shown, for proper thermalization of the microwave photons reaching the sample. Input and output paths are separated using a circulator from Quinstar (OXE89 CTH0408KC) before the device. Amplification is done by a Low Noise Factory amplifier (LNF-LNC0.3_14A) attached to the 4 K plate of the fridge. Attained base temperature at sample is 20 mK. The temperature of the sample varies a bit 10-20 mK, so we use the upper range of the temperature. The superconducting coil around the sample is used to apply magnetic field. The measurements are done using an Anritsu (MS46122B) vector network analyzer (VNA). Fig. S1 (b) shows a lumped element equivalent to the device. Note that, because of the signal propagating through the cables, an electrical length dependent phase factor gets multiplied to $S_{11}(f)$ from the device, giving a modified reflectivity $S_{11,\text{mod}}(f) = S_{11}(f) \exp(i 2\pi f \frac{L}{v_p})$ where L is the effective length traversed by the signal and v_p is the effective phase velocity of the signal. This electrical length dependent phase part, being a monotonic function of

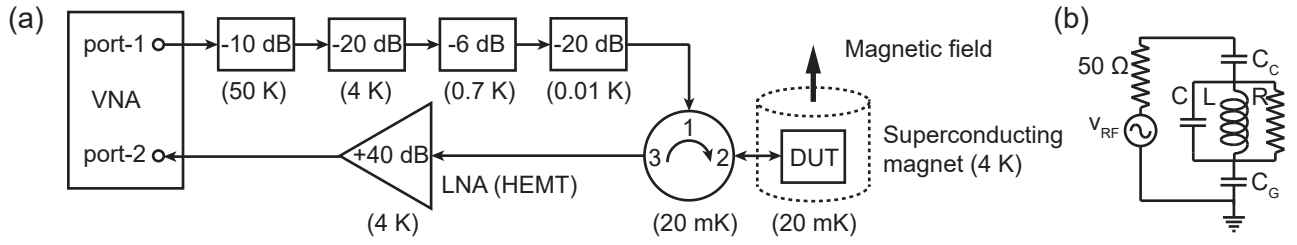


FIG. S1. (a) Circuit schematic for reflection measurement of NbN SCPW resonators in an Oxford Triton dilution fridge. RF signal from one port of a VNA is carried through a coax line with attenuation at different temperature plates inside the fridge and to the device under test (DUT) through a circulator. Reflected signal from the device is amplified by a Low Noise Factory HEMT amplifier at 4 K plate before sending it back to the other port of the VNA. (b) A lumped element equivalent of the device. Here the parallel combination of L , C and R represent the resonator, C_C represents the coupling capacitor, C_G is a capacitor representing the open-to-ground configuration of the one-port resonator and v_{RF} represents the VNA, which is used for actuation and measurement of the resonator.

frequency, adds a slope to the background of the phase of the measured signal. Hence, this shows up in the plots of real and imaginary parts of S_{11} as well. By correcting for this overall slope in the background, the pure device response is extracted. We use the functionality available in the VNA to correct for the electrical length while recording data.

SII. COMPARISON BETWEEN OVERCOUPLED AND UNDERCOUPLED RESONATORS

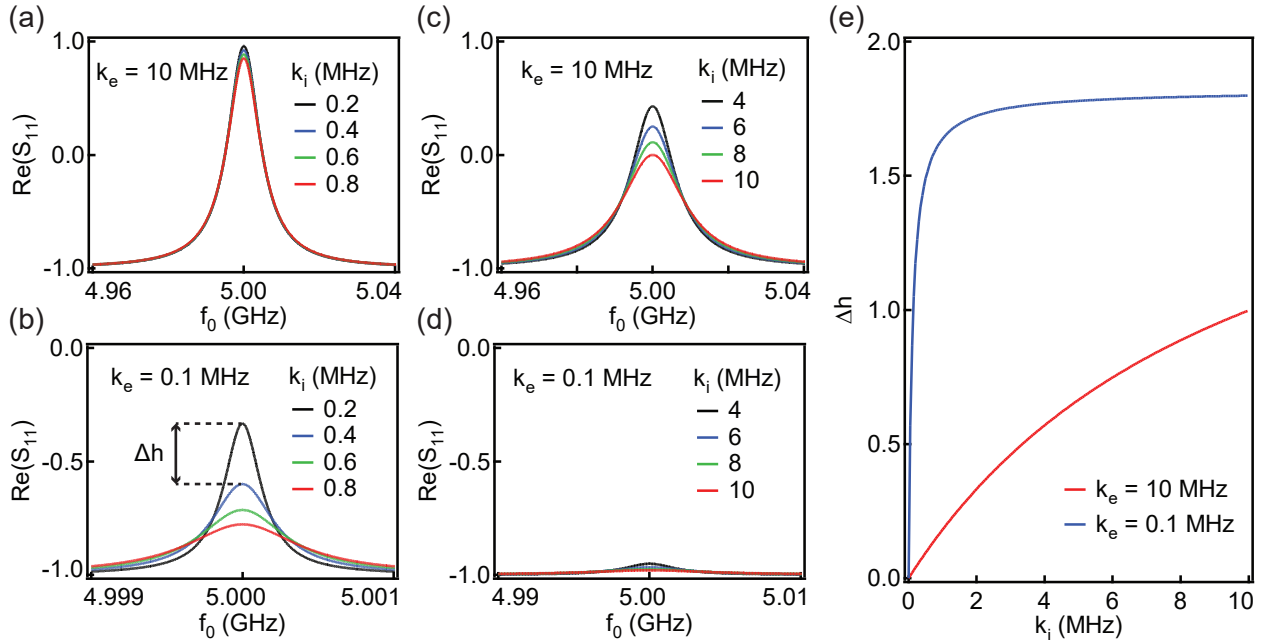


FIG. S2. Numeric calculations showing shift in peak height Δh of real part of S_{11} . (a) and (b) show Δh in high Q_i (low k_i) regime for resonator designs with low ($k_e = 10$ MHz) and high ($k_e = 0.1$ MHz) Q_e values respectively (i.e. overcoupled and undercoupled respectively). (c) and (d) show Δh in low Q_i (low k_i) regime for resonators with these two designs respectively. (e) shows a comparison between these two designs of k_e at different k_i . From these plots we observe that an overcoupled design is preferable for good fit in low Q_i regime and an undercoupled design is preferable for good fit in high Q_i regime.

Proper designing of coupling capacitor (C_C) is essential in extracting internal Q of the resonators accurately in regimes with different internal loss rates. Reflection coefficient (S_{11}) of a one-port resonator as a function of frequency is given by

$$S_{11}(f) = 1 - \frac{k_e}{\frac{k_i + k_e}{2} + i(f - f_0)} \quad (\text{S1})$$

where $k_i = \kappa_i/2\pi$ and $k_e = \kappa_e/2\pi$ are internal and external loss rates respectively and $f_0 = \omega_0/2\pi$ is the resonance frequency of the resonator. [6] They are related to internal Q (Q_i) and external Q (Q_e) by $Q_i = \frac{\omega_0}{\kappa_i} = \frac{f_0}{k_i}$ and $Q_e = \frac{\omega_0}{\kappa_e} = \frac{f_0}{k_e}$. Note that an overall constant phase factor to S_{11} with 0 or π phase can give rise to a dip or peak respectively in the real part of S_{11} , which are equivalent. For understanding effect of chosen Q_e in accuracy of extracted Q_i using Eq. (S1), we do numeric calculations in Mathematica, as shown in Fig. S2. Greater shift in peak height (Δh) of real part of S_{11} for same Q_i variation provides higher accuracy in estimation of Q_i . Fig. S2 (a) and (b) show variation in Δh in high Q_i (i.e. low k_i) regime for high (10 MHz) and low (0.1 MHz) values of chosen k_e respectively. For the higher values of Q_i considered in Fig. S2, these correspond to overcoupled ($Q_i > Q_e$) and undercoupled ($Q_i < Q_e$) designs respectively. High Q_i regime is realized near base temperature of 20 mK and zero magnetic field. Fig. S2 (c) and (d) show variation in Δh in low Q_i (i.e. high k_i) regime for these two choices of k_e . Low Q_i regime is realized as losses are introduced in the system due to increase in temperature and/or magnetic field. Fig. S2 (e) shows a comparison between $k_e = 10$ MHz and $k_e = 0.1$ MHz in terms of variation of Δh with k_i . From these panels we note that in the high Q_i regime undercoupled design (low k_e with $k_e < k_i$) is preferable for good fit, whereas in the low Q_i regime overcoupled design (high k_e with $k_e > k_i$) is preferable for good fit. We use resonators with $Q_e \approx 400$ and $Q_e \approx 22000$ for characterization of the resonators. We find that although lower Q_e is useful for extracting Q_i up to higher magnetic fields it gives high errorbars in the lower magnetic fields. Whereas, using higher Q_e enables us to extract Q_i with higher accuracy in low magnetic field regime, as implied by much lower error bars as shown in main text (Fig.4). This agrees with our comparison in Fig. S2.

SIII. SIMULTANEOUS FITTING TO REAL AND IMAGINARY PARTS OF S_{11}

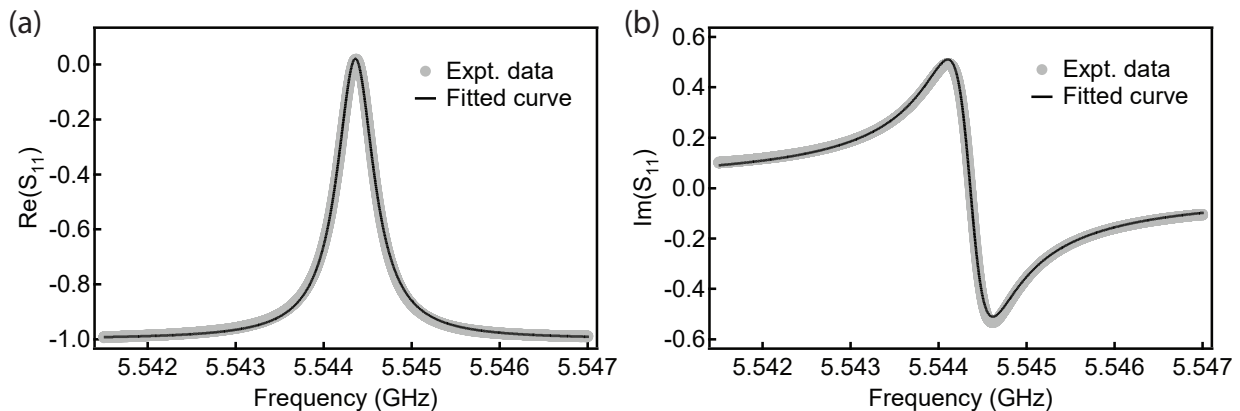


FIG. S3. (a) and (b) Simultaneous fit to real and imaginary parts of S_{11} respectively, of normalized experimental data for an NbN SCPW resonator at zero magnetic field and 20 mK base temperature using Eq. S1.

We have extracted system parameters by fitting to the real part of S_{11} data using Eq. S1. Simultaneous fitting to both real and imaginary part of S_{11} is also possible for slight improvement. Fig. S3 (a) and (b) show the simultaneous fits to real and imaginary parts of normalized S_{11} obtained from measurement of a resonator with $Q_e \approx Q_i \approx 22000$; this is close to the value obtained by fitting only to the real part of S_{11} as mentioned in main text. Further improvement can be done by implementing ways of continuous background calibration during magnetic field sweep to eliminate the background, which shows slight variation with increasing magnetic field, from the measured signal.

SIV. COMPARISON WITH PREVIOUS REPORTS

TABLE SI. Comparison of Q_i variation with magnetic field with previous reports

Material	Resonator geometry	Flux trapping scheme	Max B_{para} (for $Q_i > 10^3$)	Max B_{perp} (for $Q_i > 10^3$)
Nb [40]	SCPW	No	2.7 T (loaded $Q > 10^3$)	24 mT (loaded $Q > 2.5 \times 10^4$)
NbTiN [30]	SCPW	Yes	6 T ($Q_i > 10^5$)	45 mT (20 mT for $Q_i > 10^5$)
NbTiN nanowire [42]	Nanowire	No	6 T ($Q_i > 2 \times 10^5$)	400 mT ($Q_i > 10^4$)
NbN (our work)	SCPW	No	1 T	100 mT

Table SI shows a comparison of highest applied magnetic field, in orientations parallel and perpendicular to the SCPW plane, up to which $Q_i > 10^3$ is retained, with previous reports for other type-II superconductors. We observe that even in absence of any substrate surface treatment and flux trapping schemes, our NbN resonators retain $Q_i > 10^3$ up to parallel fields comparable to and perpendicular field twice the maximum value reported previously for an SCPW resonator. Further implementation of substrate surface treatments and flux trapping schemes are expected to increase this maximum field of high Q_i retention even more.

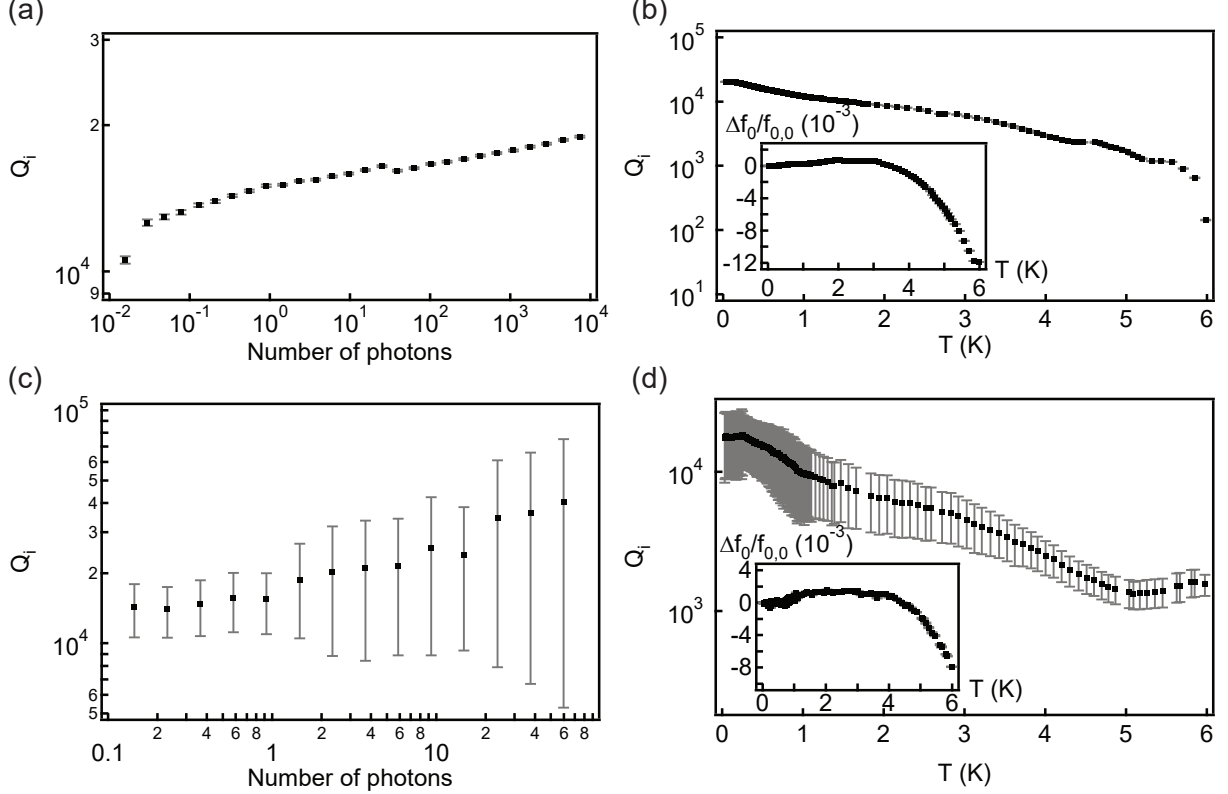


FIG. S4. Characterization of NbN SCPW resonators as a function of microwave power and temperature. (a) and (b) Variation of Q_i with increasing number of microwave photons and temperature, respectively, for intrinsic silicon substrate [Inset of (b): Variation of $\Delta f_0/f_{0,0}$ with temperature for the same]. Note that the error-bars are of size comparable to the markers. (c) and (d) Same for resonators on a sapphire substrate.

SV. CHARACTERIZATION OF RESONATORS WITH MICROWAVE POWER AND TEMPERATURE

For characterizing the fabricated resonators with respect to experimental parameters, we study the internal loss of the resonators by varying experimental conditions such as drive power and temperature. Dependence of resonance characteristics on P_{RF} is performed to investigate the performance of these resonators at and below single photon power level. The microwave power dependence of Q_i is shown in Fig. S4 (a) for intrinsic silicon substrate and in Fig. S4 (c) for sapphire substrate. From Fig. S4 (a) and (c) we observe a small increasing trend in Q_i as the mean number of microwave photons in the cavity is increased. Such a behavior suggests the presence of two-level systems (TLS). [51] At higher power, TLS get saturated and result in higher Q_i . For all the magnetic field dependent measurements discussed in the manuscript, we use a measurement power equivalent to approximately 10^3 photons in the resonator. Temperature dependence of the Q_i has been shown in Fig. S4 (b) for intrinsic silicon substrate and in Fig. S4 (d) for sapphire substrate (the insets show temperature dependence of $\frac{\Delta f_0}{f_{0,0}}$). As a general trend, above $T \approx 4$ K f_0 of the resonators show a downward shift. This reduction in f_0 can be attributed to the increasing kinetic inductance due to reduction in the number density of available Cooper pairs. Furthermore, for the same reason, increase in number density of quasiparticles causes internal losses to increase, thereby lowering Q_i . A downward shift in the relative frequency shift below $T \approx 1.5$ K confirms the presence of TLS. [51]

SVI. CHARACTERIZATION OF RESONATORS ON SAPPHIRE SUBSTRATE WITH MAGNETIC FIELD

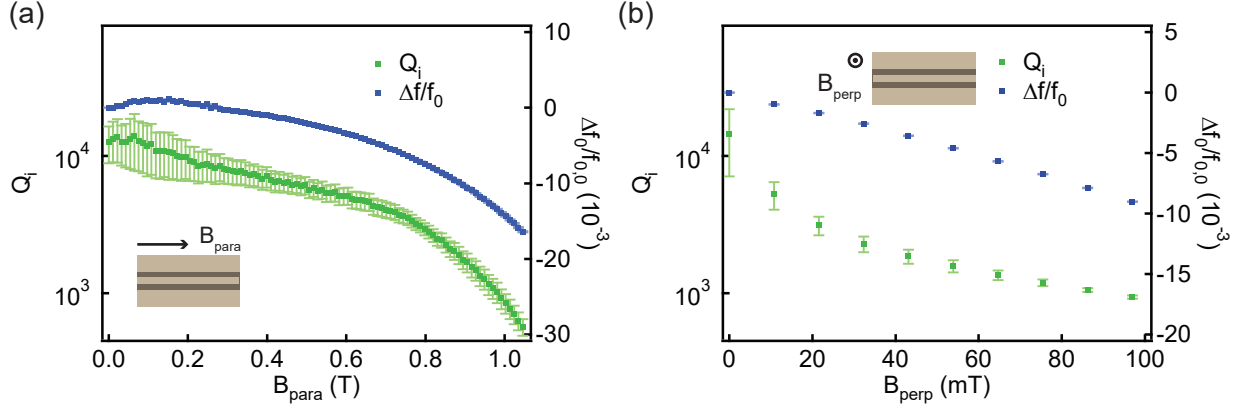


FIG. S5. Characterization of an NbN SCPW resonator on sapphire substrate (NbN film thickness 94 nm) as a function of magnetic field. (a) and (b) Variation of Q_i and $\Delta f_0/f_{0,0}$ for parallel and perpendicular field orientations respectively.

Fig. S5 (a) and (b) show variation of Q_i and $\Delta f_0/f_{0,0}$ with magnetic field parallel (B_{para}) and perpendicular (B_{perp}) to the SCPW plane respectively. This dependence is similar to that of resonators on intrinsic silicon substrate as shown in main text.

SVII. VARIATION IN $\Delta f_0/f_{0,0}$ WITH MAGNETIC FIELD FOR RESONATORS ON INTRINSIC SILICON SUBSTRATE

Fig. S6 (a) and (b) show the variation of $\Delta f_0/f_{0,0}$ for resonators on intrinsic silicon substrate with film thicknesses 217 nm and 72 nm with magnetic field parallel and perpendicular to the SCPW plane respectively. These show the nearly quadratic and linear dispersion of resonance frequency in parallel and perpendicular magnetic field respectively. The slope of the linear dispersion has been used to calculate electronic diffusion constant D . Fig. S6 (c) and (d) show the same for resonators with undercoupled design.

SVIII. HYSTERESIS WITH MAGNETIC FIELD

We observe some amount of hysteresis in the NbN SCPW resonators depending upon the direction of magnetic field sweep. Fig. S7 (a) and (b) show hysteresis in Q_i of a resonator on intrinsic silicon substrate. We observe that for the perpendicular field, Q_i is higher in down-sweep of field compared to the up-sweep; whereas, for the parallel field, we observe regimes with higher as well as lower Q_i in down-sweep compared to up-sweep. The perpendicular field case is similar to previous report and is similar to prediction from Norris-Brandt-Indenbom (NBI) model with inhomogeneous current density. [52] But the presence of two regimes in case of parallel field sweep suggests the presence of grain boundaries [53, 54] in the NbN film, which is also apparent from the SEM image of an NbN film as shown in the inset of Fig.1 in the main text.

SIX. LINEAR FIT FOR FINDING D

The electronic diffusion constant (D) is given by $D = \frac{8k}{\pi e} \frac{\beta^2 k_B T_C}{\beta^2 - f_0^2 L_g}$ as described in main text, where k is the negative of slope of the $\frac{\Delta f_0}{f_{0,0}}$ vs B_{perp} plot. Fig. S8 shows a linear fit to the $\frac{\Delta f_0}{f_{0,0}}$ vs B_{perp} data for an NbN SCPW resonator on intrinsic silicon substrate. The estimated electronic diffusion constant is $D = 5.01 \times 10^{-4} \text{ m}^2 \text{ s}^{-1}$.

SX. TRANSMISSION SPECTROSCOPY OF CHROMIUM TRICHLORIDE

Chromium trichloride (CrCl_3) is a van der Waals antiferromagnet with weak interlayer exchange. Fig. S9 (a) shows the crystal structure of CrCl_3 . The localized magnetic moments in CrCl_3 are provided by the Cr^{3+} ions shown as black spheres. In any atomic layer of CrCl_3 , the magnetic moments are in plane, shown by blue arrows, and are coupled by ferromagnetic

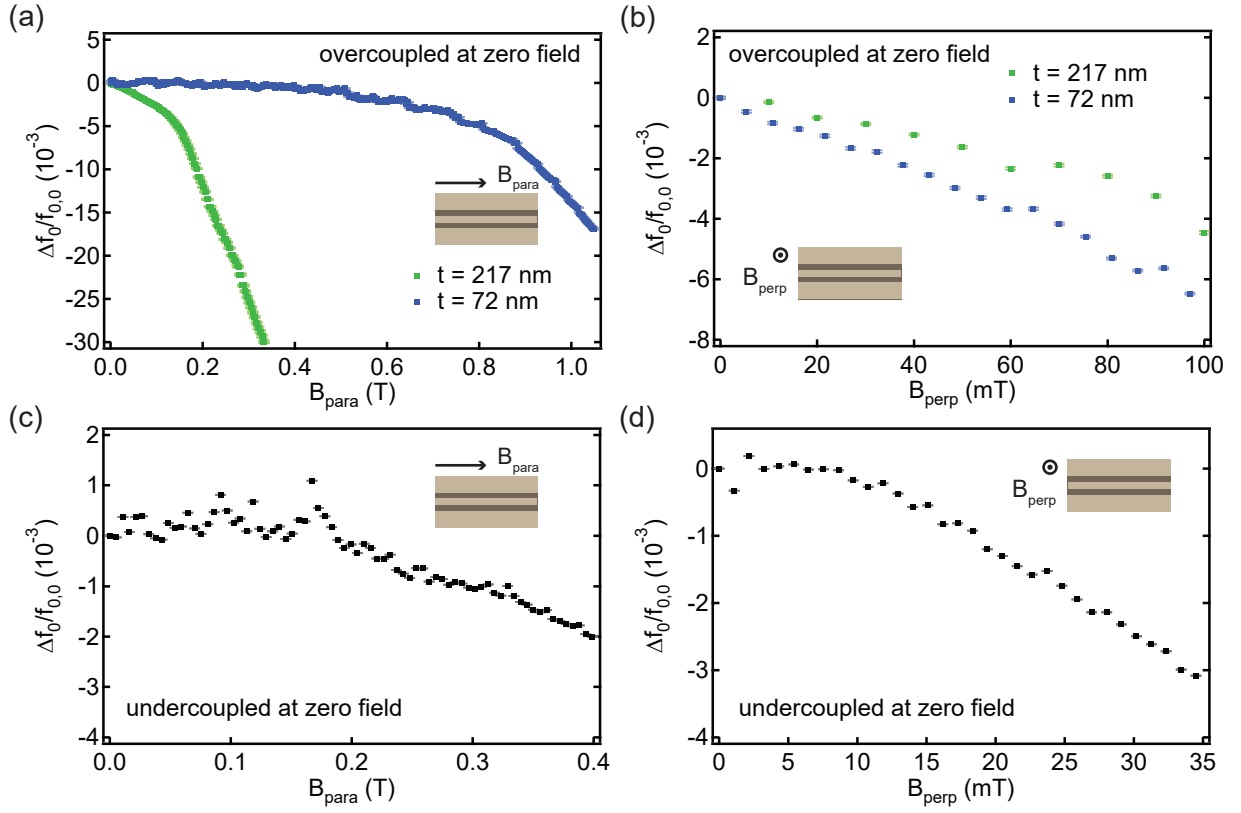


FIG. S6. Relative shift in resonance frequency $\Delta f_0/f_{0,0}$ of NbN resonators on intrinsic silicon substrate. (a) and (b) Variation in $\Delta f_0/f_{0,0}$ for the overcoupled resonators with NbN film thicknesses 217 nm and 72 nm in parallel and perpendicular magnetic field respectively. (c) and (d) Variation in $\Delta f_0/f_{0,0}$ for the undercoupled resonators with NbN film thickness 80 nm in parallel and perpendicular magnetic field respectively.

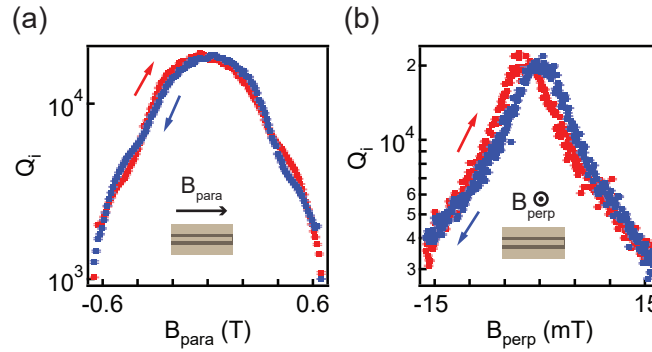


FIG. S7. Hysteresis in NbN SCPWs with magnetic field. (a) and (b) Hysteresis in an NbN SCPW resonator on intrinsic silicon substrate with respect to direction of magnetic field sweep, with field parallel and perpendicular to the SCPW respectively.

exchange. Magnetic moments in consecutive planes are antiferromagnetically coupled. Due to weak interlayer exchange of $1.6 \mu\text{eV}$, antiferromagnetic resonance (AFMR) is observed at GHz frequencies in CrCl_3 whereas, most antiferromagnets have resonance modes in THz frequency range. This allows realization of coupling of the AFMR modes in CrCl_3 with cavity modes in coplanar waveguide resonators operating in the low GHz frequencies.

To study the transmission spectra of CrCl_3 , the crystal flake was placed on a copper CPW transmission line PCB and secured with Apezion grease to protect it from ambient. The measurement was done in a He flow cryostat. As shown in Fig. S9 (b), using a vector network analyzer, microwave signal was sent from port-1 to the transmission line and the transmitted signal was amplified before being received at the port-2 of the VNA. DC magnetic field was applied parallel to the plane of the PCB and perpendicular to the segment of the transmission line containing the CrCl_3 crystal (i.e. perpendicular to the RF current at the position of the CrCl_3). The transmission spectra was obtained by measuring $S_{21}(f)$ at each value of DC magnetic field as it

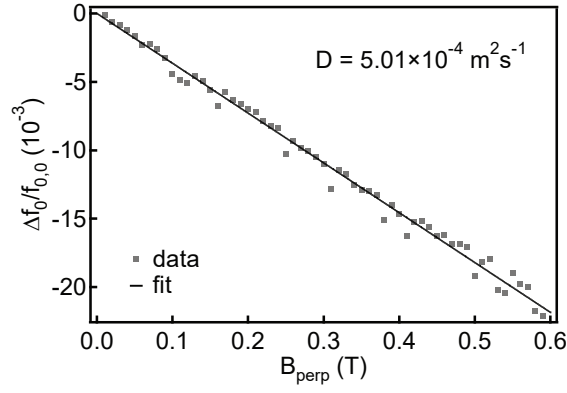


FIG. S8. Linear fit to the $\frac{\Delta f_0}{f_{0,0}}$ vs B_{perp} data for determination of electronic diffusion constant (D) for an NbN SCPW resonator on intrinsic silicon substrate.

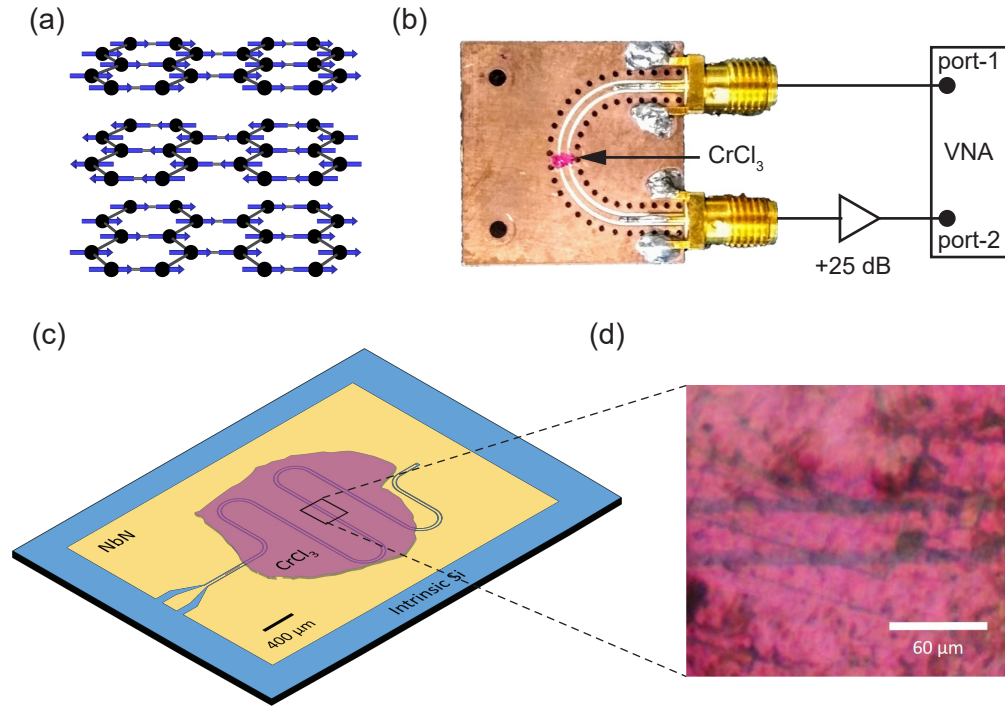


FIG. S9. (a) Crystal structure of CrCl_3 shows van der Waals stacking of antiferromagnetically oriented consecutive atomic layers (black spheres denote the Cr^{3+} ions and blue arrows depict associated moments). (b) Measurement schematic for the transmission spectroscopy of a CrCl_3 crystal flake placed on a transmission line made of copper on a PCB. (c) Schematic showing a CrCl_3 crystal flake placed on the central part of an NbN SCPW resonator for the magnon-photon coupling measurement. (d) Optical microscopy image of the crystal in the part shown by a rectangle in (c).

was swept up starting from zero field. The derivative of the transmission spectra with respect to the DC magnetic field was then plotted against the magnetic field and frequency, as shown in Fig. 4(a) of the manuscript. Using the derivative divide method,[44] the background signal can be removed from the transmission spectra without calibration of the microwave circuits. This data can then be fit to an anti-Lorentzian to determine the linewidths of the modes. A detailed study of the different modes seen in CrCl_3 is presented in ref [34] and [36].

Fig. S9 (c) shows the schematic of CrCl_3 crystal flake placed on an NbN SCPW resonator and Fig. S9 (d) shows the optical microscopy image of the grease covered CrCl_3 crystal on the NbN resonator at the current antinode of the resonator (the part shown by a rectangle in Fig. S9 (c)). As the crystal covers the entire NbN resonator, the effective volume of interaction between the microwave photons in the NbN resonator and the magnons in CrCl_3 is determined mainly by the mode volume of the

magnetic component of the RF field of the resonator.

SXI. FIT TO MAGNON DISPERSION

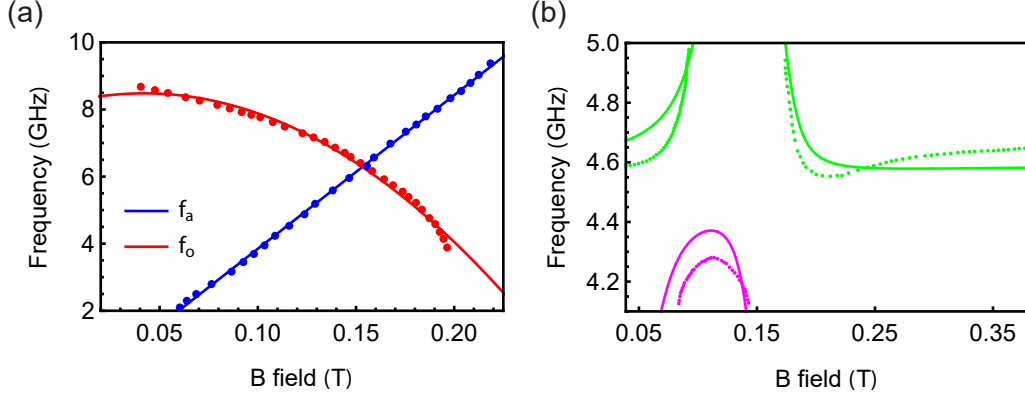


FIG. S10. (a) Polynomial fit (solid lines) to magnetic field dispersions of bare acoustic and optical AFMR modes for CrCl₃ crystal flake placed on copper transmission line. (b) Non-linear model fit to mode dispersion corresponding to magnon-photon coupling data of Fig.4(b) of the manuscript using magnetic field dependent functional form of the eigenmodes of three mode coupling Hamiltonian matrix (the dots represent the experimental data and the solid lines represent the fit).

The reflection coefficient (S_{11}) for the system with two non-interacting magnon modes coupled with a cavity photon mode can be written according to input-output theory [14, 45, 46] as

$$S_{11}(f) = 1 - \frac{k_e}{i(f - f_0) + \frac{k_i + k_e}{2} + \frac{|g_1/(2\pi)|^2}{i(f - f_1) + \frac{\gamma_1/(2\pi)}{2}} + \frac{|g_2/(2\pi)|^2}{i(f - f_2) + \frac{\gamma_2/(2\pi)}{2}}} \quad (\text{S2})$$

From Eq.S2 we can obtain the functional form for $S_{11}(B, f)$ in case of CrCl₃ placed at current antinode of an NbN resonator, by inserting the dispersion relation of each mode with magnetic field. As the B field for this measurement is parallel to the plane of the SCPW resonator, the dispersion of cavity resonance frequency (f_0) can be taken to be constant within the field range of interest for observing magnon-photon coupling. We take this to be $f_0 = 4.6$ GHz. For k_i and k_e , we use the corresponding zero field values for the cavity (at zero field, cavity and AFMR modes are off-resonance), $k_i = \frac{\kappa_i}{2\pi} = 0.0064$ GHz and $k_e = \frac{\kappa_e}{2\pi} = 0.0145$ GHz. For the field dependent functional form of the acoustic (f_1) and optical (f_2) AFMR mode frequencies in CrCl₃, we fitted linear and quadratic polynomials respectively to their field dispersions obtained from the transmission spectroscopy measurement using copper transmission line. Also, for the linewidths of the AFMR modes, we used $\frac{\gamma_1}{2\pi} = 0.33$ GHz and $\frac{\gamma_2}{2\pi} = 0.42$ GHz, as their variation with magnetic field is small. [36] This fitting is shown in Fig. S10(a). For estimation of the coupling strengths, we used a three mode coupling Hamiltonian matrix, whose elements are described in the manuscript. Using magnetic field dependent functional form of the eigenvalues of this matrix, we did a non-linear model fitting to the mode dispersions of Fig.4(b) of manuscript. This fitting gives $\frac{g_1}{2\pi} = 0.57$ GHz and $\frac{g_2}{2\pi} = 0.37$ GHz. The fitting has been shown in Fig. S10(b). From Fig.4(b) of the manuscript, we note that there is a slight downward shift in cavity resonance frequency with increasing field, in the range 0 - 0.038 T which could possibly be attributed to change in magnetic state of CrCl₃ as it undergoes spin-flop transition. [48–50] Beyond this transition, initially antiparallel spins get in canted orientation with higher fields and give rise to net magnetic moment. We fit the data between 0.038 T and 0.380 T. The cooperativity has been calculated using these values as mentioned in the manuscript. We note that all the features of the observed data are not captured by the model considered. For further understanding some aspects of the data, a microscopic modeling and more detailed analysis is required.

As the crystal covers the entire SCPW resonator, the effective volume of interaction between the magnons and the microwave photons is essentially determined by the mode volume of the magnetic component of the RF field associated with the resonator. This mode volume can be calculated using the formula $V_{\text{SCPW}} = \frac{E_{\text{SCPW}}}{2\mu_0 B_{\text{max}}^2}$, where E_{SCPW} is the energy stored in the magnetic field of the SCPW resonator and B_{max} is the maximum RF magnetic field of the SCPW resonator. We performed COMSOL simulation of the resonator to find E_{SCPW} and B_{max} , which gives a magnetic mode volume approximately 0.006 mm^3 for the SCPW resonator. Furthermore, using the lattice parameters[49] of CrCl₃ and the magnetic component of the vacuum RF field of the SCPW resonator[38, 47], we calculate the magnon-photon coupling strength per spin to be $g_0 = 7.93$ Hz and corresponding net coupling strength for the mode volume considered to be $g = g_0\sqrt{N} = 1.09$ GHz, where N is the total number of spins in

the considered volume. Better understanding of the difference between $\frac{g}{2\pi}$ that are experimentally obtained, 0.57 GHz and 0.37 GHz for the acoustic and the optical modes respectively, and the estimate of 1.09 GHz, requires microscopic magnetic modeling. Furthermore, the coupling strengths associated with the acoustic and the optical magnons depend on exact geometry and symmetry, and hence a more accurate calculation taking into account symmetry and microscopic details is required for proper estimation for the coupling strengths.